ICAS 2016
30th Congress of the International Council of the Aeronautical Sciences
DCC, Daejeon, Korea ; September 25-30, 2016

MODELING AND CONTROL OF HIGHLY FLEXIBLE FLYING-WING UAV WITH MULTIPLE ELEVONS AND PROPELLERS

Rui Wang*, **, Xiaoping Zhu, Zhou Zhou*, **, Zhengping Wang *, ****
*** College of Aeronautics, Northwestern Polytechnical University, Xi'an 710072, China,**
**** Science and Technology on UAV Laboratory, Northwestern Polytechnical University, Xi'an 710065, China**

Keywords: *highly flexible, pitch control, wing deformation, roll control reversal, heading augmentation stability by propellers*

Abstract

A coupled and geometrically nonlinear structural/flight dynamics model with unsteady aerodynamics model is developed for a large scale highly flexible solar-powered UAV. Based on the model, the UAV is trimmed with all the all-wing span elevons deflecting conformably. For the longitudinal control, the equation of motion in trimming condition is linearized firstly, then the dynamic model of elevons servo and integral signals are augmented into the control plant. The LQG/LTR method is employed to control the pitch angle. Simulation results show that the controller can provides a quick dynamic response with a very small additional deformation of the wing. For lateral-directional control, the lateral control efficiency of elevons is evaluated. It is found that due to the large lateral and poor directional static stability, the lateral control efficiency is very limited, and an aileron reversal coefficient is proposed and verified. In contrast, the multi-lateral differential throttles control has higher control efficiency in lat-dir control, but it must be noted that the inertia of propellers and motors will reduce the phase margin and the damping ratio of Dutch mode significantly due to the low cut-off frequency.

1 General Introduction

For a large aspect Flying-Wing (FW) solar-powered UAV, its wing is extremely light and highly flexible. These characteristics will introduce significant geometrically nonlinear aeroelastic deformation during flight, and strong coupling between aeroelasticity and flight dynamics. Not taking those issues into account is problematic.

In addition, because of the large span, multiple distributed elevons and propellers are usually employed, but their control efficiency are quite low due to relatively small size and power. So, it's a challenge to control the UAV optimally with such a limited control ability under the influence of both the strong coupling of flight/structural dynamics in small stability margin and significant aeroelasticity.

Regarding to the modeling of highly flexible vehicles, fruitful works have been presented by Hodges, Cesnik and their co-workers. The analysis method presented by Hodges et al has developed into NATASHA (Nonlinear Aeroelastic Trim And Stability of HALE Aircraft), a computer program that is based on geometrically exact, fully intrinsic beam equations and a finite-state induced flow model [1-4]. The University of Michigan's Nonlinear Aeroelastic Simulation Toolbox (UM/NAST) is developed by Cesnik and his co-workers [5-6], which includes a nonlinear strain-based beam model, unsteady aerodynamics with simplified stall models and a six-degree-of-freedom flight dynamic equation. Ref. [7] presented a method where a displacement-based geometrically nonlinear flexible-body dynamics equation is coupled with a three-dimensional unsteady vortex lattice for flexible aircraft.

In the field of flight dynamics and control of highly flexible UAV, ref. [1] found that the behavior is distinctly different from that of a rigid aircraft while taking into account the flexibility effects. Because the low-frequency modes of structure are completely coupled to the flight dynamics mode, the phugoid and the short period mode are affected by the wing flexibility significantly. Ref. [2] presented a theoretical basis for the flight dynamic response estimation of a highly flexible flying wing, where multiple engines, and multiple control surfaces are taken into account. Ref. [8] shows that, the flexible model is the only one which is able to accurately estimate the longitudinal flight dynamics behaviors, but the deformed model is quite accurate for lat-dir flight dynamics analysis. For the lateral control, the aileron was employed to level turning control in Ref. [3], but the heading moment of aileron was not considered, which might cause large errors. In Ref. [9], the principle of the increased heading damping of solar powered UAV caused by multi-propellers was analyzed, so was the heading control performance with differential power propellers, but the effect of the dynamic responses of the propulsion system on control performance was not considered.

The highly flexible FW UAV discussed in this paper is shown in Fig.3. It is equipped with 8 propulsion systems and 5 vertical tails. The span is 70m and the mean aerodynamics chord (MAC) is 2.44m. In order to mount adequate solar arrays for the purpose of long endurance, the control surface has to be compressed to the 5% trailing edge as an elevon. In order to enhance the control ability, the trailing-edge elevon spans the entire wing. The elevon is divided into 40 dependent parts to release the notable aeroelastic deformation caused by the large scale and the highly flexibility. The diameter of each propeller is 1.65m, and their max rotation speed at sea level is 800 rpm.

The objective of this paper is to find an effective method to model the dynamics of the proposed UAV for trimming and control, propose a rational method for the longitudinal control with the high coupling of structural/flight dynamics, and develop an effective lat-dir control method in the influence of weak stability and controllability of solar-powered UAV with multiple elevons and propellers.

2 Structural and Flight Dynamics Coupling Model

2.1 Geometrically Nonlinear Structural Dynamics

The intrinsic beam equation derived by Hodges et al is employed to model the geometrically nonlinear structural dynamics and flight dynamics equations of this highly flexible FW UAV, which is shown as follows [2]:

$$
\begin{aligned}
&\dot{\bar{P}} + \tilde{\bar{\Omega}}\bar{P} = F' + \tilde{\bar{K}}\bar{F} + \bar{f} \\
&\dot{\bar{H}} + \tilde{\bar{\Omega}}\bar{H} + \tilde{\bar{V}}\bar{P} = M' + \tilde{\bar{K}}\bar{M} + (\tilde{e}_2 + \tilde{\bar{\gamma}})\bar{F} + \bar{m} \\
&\dot{\bar{\gamma}} = V' + \tilde{\bar{K}}\bar{V} + (\tilde{e}_2 + \tilde{\bar{\gamma}})\bar{\Omega} \\
&\dot{\bar{\kappa}} = \Omega' + \tilde{\bar{K}}\bar{\Omega} \\
&\dot{\hat{P}} + \tilde{\hat{\Omega}}\hat{P} = \hat{f} \\
&\dot{\hat{H}} + \tilde{\hat{\Omega}}\hat{H} = \hat{m}
\end{aligned}
\tag{1}
$$

The details of the equation set above can be seen in ref. [2]. Eq.(1) is the core of structure dynamics, but it cannot be used for the analysis of aerodynamics and flight dynamics without the relationship of displacements and rotations. Hence, the kinematics motion must be established to obtain the relationship between the strain and the displacement of the wing. The position vector of the origin of the deformed beam frame (*B*-) is in the root frame (*R*-) and their rotational relationship are [10]:

$$
\begin{aligned}
&\{r_B\}_R = C_{RB}(\gamma + e_2) \\
&C_{BR}{}' = -(\tilde{\kappa} + \tilde{k})C_{BR}
\end{aligned}
\tag{2}
$$

In order to validate the effectiveness of the geometrically nonlinear structural model, a cantilever beam with bending rigidity EI =1 and length l =1 m are employed. While applying increasing moment M at the tip of the beam, the deformation of the beam is shown in the following figure. It can be seen that, while $M = 2\pi$, the angular displacement is 2π, the tip coincides with the root and the beam is deformed into a circle, which is consistent with the analytical results. The effectiveness of structural model is validated.

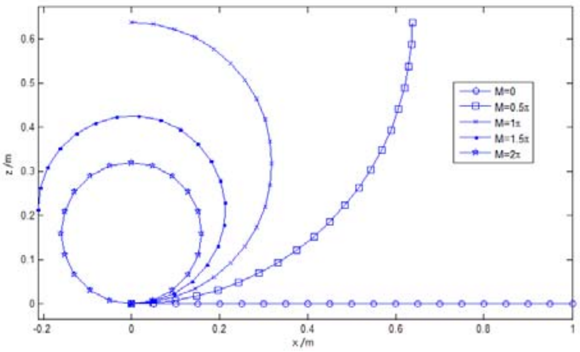

Fig.1 Beam deformation with increasing tip moment

2.2 Unsteady Aerodynamics Model

In order to analyze the motion of the flexible UAV exactly, the unsteady effect due to the large deformation should be included in the aerodynamic model. The two most well-known unsteady aerodynamic models are Theodorsen unsteady aerodynamic model and the finite state induce flow model [10]. The Theodorsen model is derived in the frequency domain, but it can be converted into the time domain by rational function approximation. The finite state induce flow model is derived in the time domain, and it can be used in a state-space model easily. These two types of aerodynamics are equivalent and can be derived from one another through Laplace and Fourier transforms.

In this paper, the Theodorsen unsteady aerodynamics model is adopted, and the Roger's approximation is employed to convert it from the frequency domain into the time domain form.

The Theodorsen unsteady aerodynamic model can be found in ref. [11]. It also can be rewritten as matrix form for the convenience of programming as follows:

$$
\begin{aligned}
\begin{bmatrix} L \\ M_E \end{bmatrix} &= \frac{q}{V^2}\begin{bmatrix} 2\pi b^2 & -2\pi b^3\bar{a} \\ 2\pi b^3\bar{a} & -2\pi b^4(\frac{1}{8}+\bar{a}^2) \end{bmatrix}\begin{bmatrix} \dot{V}_z \\ \dot{\Omega}_y \end{bmatrix} \\
&+\frac{q}{V}\begin{bmatrix} 0 & 2\pi b^2 \\ 0 & -2\pi b^3(\frac{1}{2}-\bar{a}) \end{bmatrix}\begin{bmatrix} V_z \\ \Omega_y \end{bmatrix} \\
&+\frac{q}{V}\begin{bmatrix} 4\pi b & 4\pi b^2(\frac{1}{2}-\bar{a}) \\ 4\pi b^2(\bar{a}+\frac{1}{2}) & 4\pi b^3(\bar{a}+\frac{1}{2})(\frac{1}{2}-\bar{a}) \end{bmatrix} C(k)\begin{bmatrix} V_z \\ \Omega_y \end{bmatrix} \\
&+q\begin{bmatrix} C_{l0}2b \\ C_{m0}4b^2 \end{bmatrix}+q\begin{bmatrix} C_{l\delta_f}2b \\ C_{m\delta_f,e}4b^2 \end{bmatrix}\delta_f
\end{aligned}
\tag{3}
$$

where: $C(k)=F(k)+iG(k)$

The unsteady aerodynamics model presented above includes the reduce frequency k. For the purpose of applying it to the flight dynamics and control, it needs to be converted from the frequency domain to the time domain. Roger's approximation is adopted in this paper.

Because $s=i\omega$, $k=\omega b/V$, so $s=ikV/b$. Denote $\bar{s}=sb/V$, and one can derive $\bar{s}=ik$, then one can convert $C(k)$ to $C(s)$ by the Roger's approximation as follows:

$$C(s)=q_0+q_1\bar{s}+q_2\bar{s}^2+\sum_{m=3}^{6}q_m\frac{\bar{s}}{\bar{s}+\beta_{m-2}}$$

Substituting s into the above equation, one can derive:

$$
\begin{aligned}
C(k) &= q_0+q_1\frac{ikV}{b}-q_2(\frac{kV}{b})^2 \\
&+q_3\frac{\frac{kV}{b}}{\frac{kV}{b}-i\beta_1}+q_4\frac{\frac{kV}{b}}{\frac{kV}{b}-i\beta_2}+q_5\frac{\frac{kV}{b}}{\frac{kV}{b}-i\beta_3}+q_6\frac{\frac{kV}{b}}{\frac{kV}{b}-i\beta_4}
\end{aligned}
\tag{4}
$$

Roger's approximation is to solve the following equation by the fit method:

$$
\begin{aligned}
&F(k)+iG(k) \\
&= q_0+q_1\frac{ikV}{b}-q_2(\frac{kV}{b})^2 \\
&+q_3\frac{\frac{kV}{b}}{\frac{kV}{b}-i\beta_1}+q_4\frac{\frac{kV}{b}}{\frac{kV}{b}-i\beta_2}+q_5\frac{\frac{kV}{b}}{\frac{kV}{b}-i\beta_3}+q_6\frac{\frac{kV}{b}}{\frac{kV}{b}-i\beta_4}
\end{aligned}
\tag{5}
$$

Therefore, there are 11 coefficients, q_0, $q_1 \ldots q_6$, $\beta_1, \ldots \beta_4$ to be fitted. After that, substituting them into the expression of $C(s)$, then the unsteady aerodynamics can be converted to the time domain. The independent variable in Eq. (5) is k, from practice it shows that different ranges of k will influence the fitted results of coefficients greatly, therefore, it should be dense on the interested band of frequency while sparse on the other frequencies. In order to eliminate the possible complex coefficient emerging during the fit, the real and imaginary part in Eq. (5) should be fitted separately. Furthermore, q_0 is equivalent to 1 in theory, and it doesn't need to be fitted.

Substituting Eq. (5) and (4) into Eq. (3), the final expression of Theodorsen unsteady aerodynamics can be derived as follows:

$$\begin{bmatrix} L \\ M_E \end{bmatrix} = Q_c + Q_{\delta_f}\delta_f + Q_0 x + Q_1\dot{x} + Q_2\ddot{x} + \sum Q_m x_{am}$$

$$\dot{x}_{am} = \dot{x} - \frac{V}{b}\beta_{m-2}x_{am} = \dot{x} + Q_{bm-2}x_{am}, \qquad m = 3,4,5,6 \tag{6}$$

Where:

$$x = \left[V^T, \Omega^T\right]^T, \; Q_c = q\begin{bmatrix} C_{l0}2b \\ C_{m0}4b^2 \end{bmatrix},$$

$$Q_{\delta_f} = q\begin{bmatrix} C_{l\delta_f}2b \\ C_{m\delta_f,e}4b^2 \end{bmatrix}, Q_{bm-2} = -\frac{V}{b}\beta_{m-2},$$

$$Q_0 = \frac{q}{V}\begin{bmatrix} 0 & 2\pi b^2 \\ 0 & -2\pi b^3(\frac{1}{2}-\bar{a}) \end{bmatrix}$$

$$+\frac{q}{V}\begin{bmatrix} 4\pi b & 4\pi b^2(\frac{1}{2}-\bar{a}) \\ 4\pi b^2(\bar{a}+\frac{1}{2}) & 4\pi b^3(\bar{a}+\frac{1}{2})(\frac{1}{2}-\bar{a}) \end{bmatrix} q_0,$$

$$Q_1 = \frac{q}{V^2}\begin{bmatrix} 2\pi b^2 & -2\pi b^3\bar{a} \\ 2\pi b^3\bar{a} & -2\pi b^4(\frac{1}{8}+\bar{a}^2) \end{bmatrix}$$

$$+\frac{q}{V}\begin{bmatrix} 4\pi b & 4\pi b^2(\frac{1}{2}-\bar{a}) \\ 4\pi b^2(\bar{a}+\frac{1}{2}) & 4\pi b^3(\bar{a}+\frac{1}{2})(\frac{1}{2}-\bar{a}) \end{bmatrix} q_1(\frac{b}{V}),$$

$$Q_2 = \frac{q}{V}\begin{bmatrix} 4\pi b & 4\pi b^2(\frac{1}{2}-\bar{a}) \\ 4\pi b^2(\bar{a}+\frac{1}{2}) & 4\pi b^3(\bar{a}+\frac{1}{2})(\frac{1}{2}-\bar{a}) \end{bmatrix} q_2(\frac{b}{V})^2,$$

$$Q_m = \frac{q}{V}\begin{bmatrix} 4\pi b & 4\pi b^2(\frac{1}{2}-\bar{a}) \\ 4\pi b^2(\bar{a}+\frac{1}{2}) & 4\pi b^3(\bar{a}+\frac{1}{2})(\frac{1}{2}-\bar{a}) \end{bmatrix} q_m.$$

In order to improve the accuracy, actual airfoil data can be used to correct the equation above.

Using the fitting method described previously, fitting k in the range of [0, 0.5], the theoretical and calculated results are compared in Fig.2. It can be seen that the fitting method proposed in this paper is sufficiently accurate.

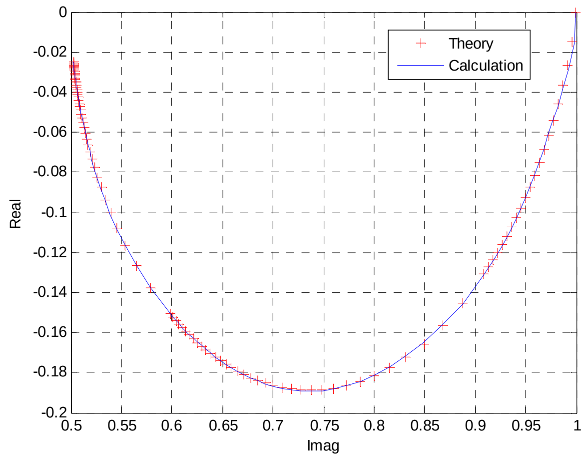

Fig.2 Fitting unsteady aerodynamics

2.3 Total Equation of Moment

A primary total equation of motion can be seen in ref. [8] and [13], after the integration of unsteady aerodynamic model presented in this paper into the equation, a nonlinear structural and flight dynamics coupling model can be derived. Trimming in large deformation and nonlinear flight control and simulation can be processed based on this model.

The final total linear equations can be obtained as follows:

$$\dot{\boldsymbol{x}}_{lon} = \boldsymbol{A}_{lon}\boldsymbol{x}_{lon} + \boldsymbol{B}_{lon}\boldsymbol{\delta} \tag{7}$$

where:

$$\boldsymbol{x}_{lon} = \left[x_r, x_{ne}, \dot{x}_{ne}, x_{na3}, \cdots, x_{naN}\right]^T$$

$$A_{lon} = \begin{bmatrix} A_{rr} & A_{rne} & 0 & A_{rna_3} & \cdots & A_{rna_N} \\ 0 & 0 & I & 0 & 0 & 0 \\ A_{er} & -\bar{M}^{-1}\bar{K} & -\bar{M}^{-1}\bar{D} & q_d\bar{M}^{-1}Q_3 & \cdots & q_d\bar{M}^{-1}Q_N \\ 0 & 0 & I & -\frac{V}{b}\beta_1 I & \cdots & 0 \\ 0 & 0 & \vdots & \vdots & \vdots & \vdots \\ 0 & 0 & I & 0 & \cdots & -\frac{V}{b}\beta_{N-2}I \end{bmatrix}$$

$$B_{lon} = \left[B_r^T, 0, B_{ne}^T, 0, \cdots, 0\right]^T$$

$$\delta = \begin{bmatrix} \delta_{ea} \\ \delta_t \end{bmatrix}$$

$$\bar{M} = M - q_d(\frac{b}{V})^2 q_2, \; \bar{D} = -q_d\frac{b}{V}q_1, \; \bar{K} = K - q_d q_0$$

The deformed model is quite accurate for lat-dir flight dynamics analysis [8]. That is:

$$\dot{\boldsymbol{x}}_{lat} = \boldsymbol{A}_{lat}\boldsymbol{x}_{lat} + \boldsymbol{B}_{lat}\boldsymbol{\delta} \tag{8}$$

where, $\boldsymbol{x}_{lat} = [\beta, p, r, \phi]^T$.

The equation above keeps the same form as the rigid equation of motion, but the aerodynamics coefficient and inertial of moment are vary as the wing deformed.

3 Longitudinal Control

3.1 Trimming

In the level flight, assuming that all the 40 distributed elevons deflect conformably for trimming for simplification, and the highly flexible UAV will deform under the aeroelastic effect. As seen in Fig.4, the maximum wing deformation is 4.58m at the wing tip. So, all the distributed elevons deflecting conformably is not the optimal control case while considering aeroelasticity.

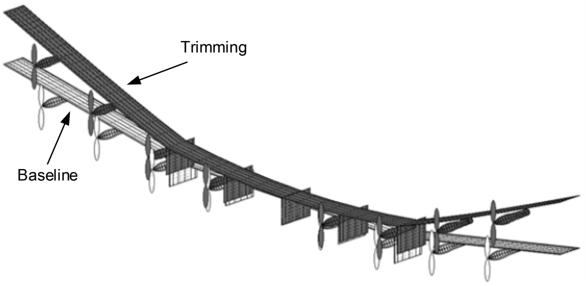

Fig.3 Deformed UAV in trimming

The displacements and pitch angles along the span are shown as follows:

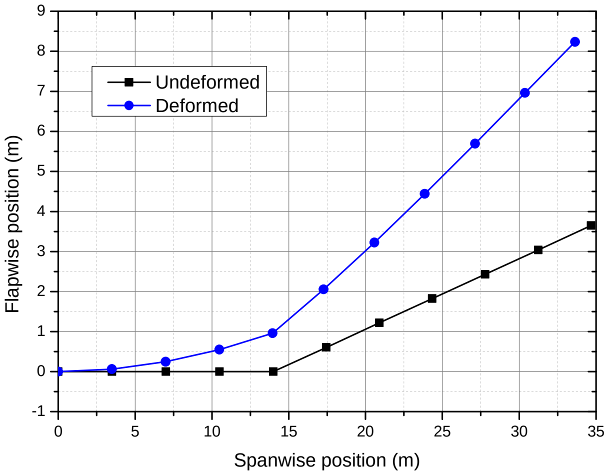

Fig.4 Flapwise position of UAV of different calculation model

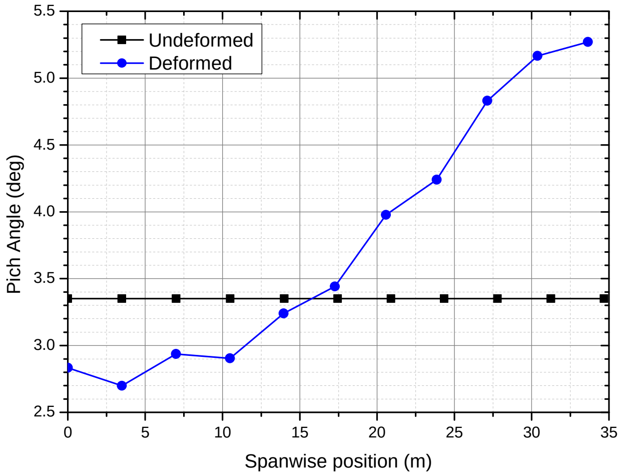

Fig.5 Pitch angle of UAV of different calculation model

It can be seen that, the maximum wing deformation is 4.58m at the wing tip, and the pitch angle at wing tip is larger than the root for about 3°. Larger pitch angle brings larger lift, and larger lift at wing tip results in larger deformation. So, the control method where all the distributed elevons deflecting conformably is not the optimal control case while considering aeroelasticity.

3.2 Longitudinal Pitch Control

Pitch control is the foundation of the longitudinal control. Since the chord of elevons are only 5% MAC, the control efficiency is very low, it needs to use the whole 40 elevons for longitudinal control, at the same time, it's necessary to maintain the wing in a reasonable small deformation. Therefore, the pitch control is a complex Multi-Input Multi -Output (MIMO) system.

In order to describe the dynamic characteristics of the UAV accurately, the longitudinal small disturbance equation of motion of Eq.(7), which contains the coupling of flight dynamics, structural dynamics and unsteady aerodynamics is employed. Furthermore, in order to accurately describe the characteristics of UAV control, the dynamic characteristics of the actuator need to be considered.

Two kinds of actuators are employed. The model of elevons actuator is:

$$\delta_{ea} = \frac{1}{0.05s + 1} u_{ea} \tag{9}$$

The model of throttles is:

$$\delta_t = \frac{1}{0.33s+1} u_t \quad (10)$$

They can be rewritten as the state-space form as follows:

$$\dot{\delta} = A_\delta \delta + B_\delta u \quad (11)$$

where, $u = [u_{ea}, u_t]^T$

Combinating Eq. (7) and (11), the longitudinal dynamic equation with actuator can be derived as follows:

$$\begin{bmatrix} \dot{\boldsymbol{x}}_{lon} \\ \dot{\delta} \end{bmatrix} = \begin{bmatrix} \boldsymbol{A}_{lon} & B_{lon} \\ 0 & A_\delta \end{bmatrix} \begin{bmatrix} \boldsymbol{x}_{lon} \\ \delta \end{bmatrix} + \begin{bmatrix} 0 \\ B_\delta \end{bmatrix} u \quad (12)$$

Before designing pitch control law, one shall augment the plant to satisfy the specific performance requirement. For example, adding integrators will assure the zero steady-state errors to step inputs. So in order to control the pitch angle precisely, the integrator of pitch angle θ_i and velocity V_i should be included in the control plant. Then, the control plant in Eq.(12) becomes:

$$\begin{bmatrix} \dot{x}_{lon} \\ \dot{\delta} \\ \dot{\theta}_i \\ \dot{V}_i \end{bmatrix} = \begin{bmatrix} A_{lon} & B_{lon} & 0 & 0 \\ 0 & A_\delta & 0 & 0 \\ [0,0,0,1] & 0 & 0 & 0 \\ [1,0,0,0] & 0 & 0 & 0 \end{bmatrix} \begin{bmatrix} x_{lon} \\ \delta \\ \theta_i \\ V_i \end{bmatrix} + \begin{bmatrix} 0 \\ B_\delta \\ 0 \\ 0 \end{bmatrix} \boldsymbol{u} \quad (13)$$

3.3 Designing the LQG/LTR Controller

LQG/LTR is a popular robust control method. The primary objective of LQG/LTR is to recover the robustness of LQG, an excellent full-state feedback robust controller. The procedure of the LQG/LTR method is as follows. Firstly, design a target feedback loop, which shall satisfy the desired frequency performance, such as disturbance rejection and uncertainty deviation of the unmolded dynamics, and then design a model based compensator to recover the properties of the target feedback loop [14]. LQG/LTR has been used widely in flight control, but only a few references are concentrated on the highly flexible aircraft.

LQG/LTR controller is based on the LQG control, which can handle optimal control problem of MIMO system well, and keep good robustness and dynamic characteristics. The LTR technology reconstructs the controller with less measurable output variables instead of state variables for feedback while keeping the robustness and dynamic characteristics of the original LQG controller. Therefore, it's possible to utilize LQG/LTR controller for the pitch control of solar-powered UAV in reality.

The critical factor for a practical controller is that, not all the state variables are easy to be measured in engineering. So only a part of variables can be used to implement the output feedback control. Because the LTR technology can recover the stable margin of LQR that is known as an excellent state feedback robust controller, the robustness of LQG/LTR output feedback controller can be guaranteed.

It's time to decide the feedback control parameters now. Because the flapwise bending and torsion motion of the wing are easy to be measured, so u_z, φ_y together with V, α, q, θ, θ_i, V_i are selected to be the measured variables for the controller. Then, we can apply the LQG/LTR method described above to Eq.(13).

When the LQG/LTR recovery gain is chosen as $\rho = 1\times10^6$, the singular values of pitch angle loop of FG(s) denoted by LQR and G_c(s)G(s) denoted by LTR are compared in the following figure:

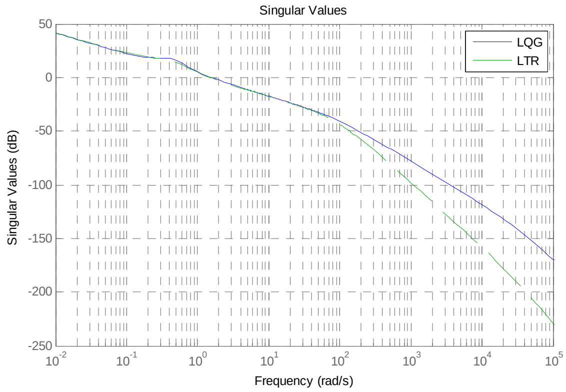

Fig.6 Singular values of pitch angle loop

It can be seen from Fig.6 that, after the loop transfer recovery, the two singular values coincide perfectly on low frequency, which indicates that the response of the close loop system to inputs such as step input is quickly. On high frequency band, the singular value of LTR decreases more quickly than that of LQR, that will provide excellent robustness to the high frequency disturbance and model deviation. So, the LTR can meet the required performance.

3.4 Flight Simulation

Applying the LQG/LTR controller proposed above to the linear structural and flight dynamics model described in Eq. (13), when given a desired pitch angle $\theta_c = 5°$, the longitudinal responses of the solar-powered UAV are shown in the following figures.

As shown in Fig.7, the adjust time of pitch angle is about 3 seconds. Because of the introduction of integrator, the steady-state error is eliminated gradually.

As shown in Fig.8, the variation of angle of attack in the whole process does not exceed 1.4°, so the additional load it brings is very small, indicating that the overall movement of the highly-flexible UAV is relatively stable.

As seen in Fig.9, the largest deflection angle of elevons is less than 20 degrees, and it only occurs in the initial phase, when approaching the steady state, the deflections are no more than 5 degrees, far less than the threshold. It must be noted that the deflection angles of the 40 elevons are all different, because in addition to providing pitch angle control, distributed elevons also need to suppress the elastic deformation movement of the highly-flexible wing in the LQG/LTR controller.

As seen in Fig.10, the maximum deformation of the wing occurs in the tip, the maximum magnitude of which is only about 0.15 m, far less than the deformation of 4.58 m in trimming, reminding that all the elevons deflect conformably in trimming.

As seen in Fig.11, the max rate of twist angle is only 0.025 rad/s, corresponding to the reduced frequency of 0.0035, which is in the range of Fig.2. In a word, with distributed elevons, the use of LQG/LTR control method allows faster attitude control of the large scale highly flexible UAV while a good aeroelastic deformation suppression is achieved simultaneously.

In addition, reminding that the linear structural model coincides with the nonlinear one perfectly in the condition of small deformation. Since the LQG/LTR controller has limited the structural deformation and incident angle to a relatively small range, it can be deduced that the simulation results in this section are reliable.

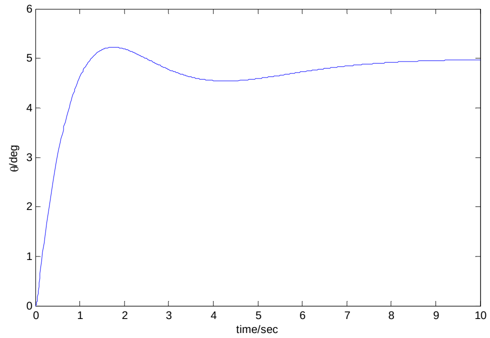

Fig.7 Response of pitch angle

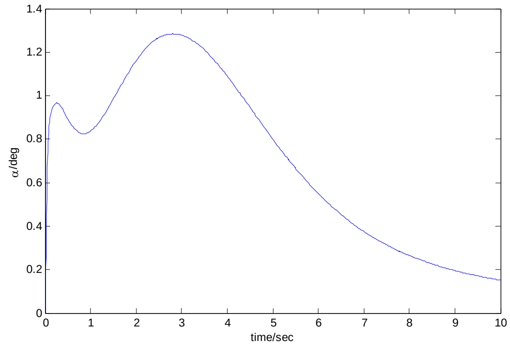

Fig.8 Response of angle of attack

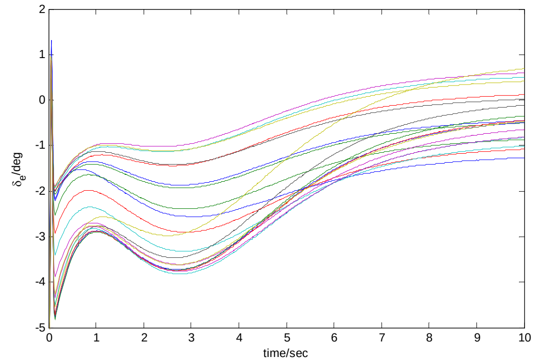

Fig.9 Response of elevons at different stations

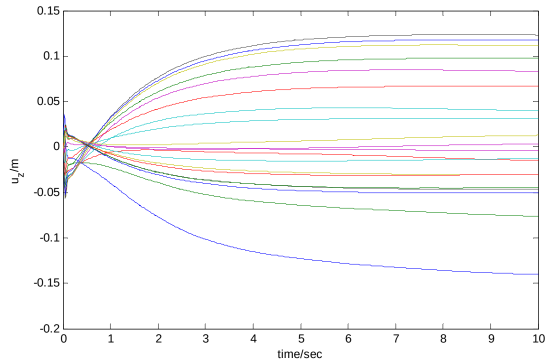

Fig.10 Response of vertical displacements of wing at different stations

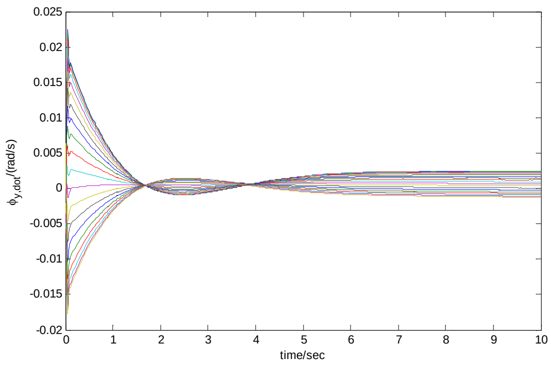

Fig.11 Response of rate of twist angle of wing at different stations

4 Lateral-Directional Control

As discussed in ref. [8], the deformed model is quite accurate for lateral-directional flight dynamics analysis of highly-flexible UAV. Therefore, the deformed model is employed to evaluate the lateral-directional controllability in this work.

4.1 Roll Control Reversal

Generally the roll control is achieved by aileron. According to Ref. [15], the transfer function from the aileron δ_a to the roll angle ϕ is formulated as:

$$\frac{\phi}{\delta_a}=\frac{\bar{L}_{\delta_a}(S^2+2\varsigma_\gamma\omega_\gamma S+\omega_\gamma^2)}{(S-\lambda_1)(S-\lambda_2)(S^2+2\varsigma_D\omega_D S+\omega_D^2)} \quad (14)$$

where λ_1 and λ_2 are eigenvalues of roll and spiral mode respectively; ς_D and ω_D are the damping ratio and frequency of Dutch mode respectively. Therefore, when the three lateral-directional modes are convergent, the sign of the ratio between the roll angle in steady-state and aileron is consistent with that of $\bar{L}_{\delta_a}\omega_\gamma^2$, where:

$$\omega_\gamma^2=\bar{Y}_\beta(\bar{N}_r-\frac{\bar{N}_{\delta_a}}{\bar{L}_{\delta_a}}\bar{L}_r)+\frac{\bar{N}_{\delta_a}}{\bar{L}_{\delta_a}}\bar{L}_\beta-\bar{N}_\beta \quad (15)$$

For the proposed large aspect FW configuration, $\bar{N}_r$ and $\bar{Y}_\beta$ are relatively small, so in the preliminary analysis, the first term of the right-hand side in the above equation can be ignored. For a normal aircraft, $\bar{L}_{\delta_a}$ <0, to make the roll induced by aileron step controlling meet the normal manipulation, the following equation must be met:

$$C_{\delta_a}=\frac{\bar{N}_{\delta_a}}{\bar{L}_{\delta_a}}\bar{L}_\beta-\bar{N}_\beta<0 \quad (16)$$

where $C_{\delta a}$ is the constant of aileron reversal. When the aileron differential deflections of both sides are equal, adverse yaw will be caused by aileron, that is, $\bar{N}_{\delta_a}$ > 0. Besides, because of the directional static instability of flying wing configuration, which means $\bar{N}_\beta$ <0, in order to obtain a normal response of aileron manipulation, differential aileron deflections of both sides should be unequal, and to make $\bar{N}_\beta$ <0 to satisfy Eq. (16).

To validate the above formula, the definition of four different states of the UAV, and the value of $C_{\delta a}$ in each state are shown in the following table:

Table 1 Define different conditions of $\bar{N}_{\delta_a}$

Condition	C1	C2	C3	C3
$\bar{N}_{\delta_a}$	0.081	0	-0.066	-0.141
$C_{\delta a}$	0.075	0.034	0	-0.038

For the 4 conditions defined in the above table, the response of roll angle ϕ under the aileron step input of 5° is shown in Fig.12. It is illustrated from the figure that, the aileron reversal is eliminated gradually while $C_{\delta a}$ becomes smaller. When $C_{\delta a}$=0, the steady state value of roll angle is approximated to 0 too, which validates the high accuracy of Eq. (16). In addition, because the dihedral angle enlarges the magnitudes of $\bar{L}_\beta$ and $\bar{N}_\beta$, the value of $\bar{N}_{\delta_a}$ should be inversely increased two times so that the control effect of aileron achieves 0.1°(ϕ)/s/°(δ_a), which is much less than the requirement of flight qualities. In contrast, multi-lateral differential throttle has higher control efficiency, which will be proven in the following section.

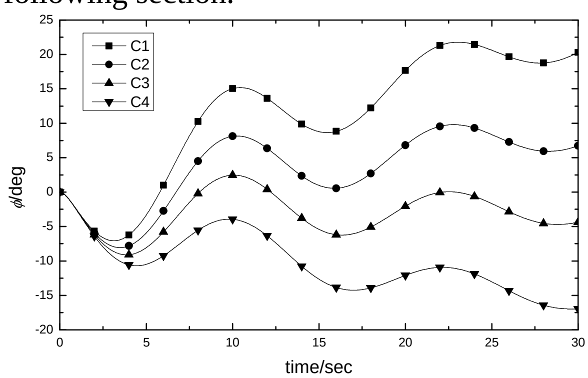

Fig.12 Response of roll angle of different $\bar{N}_{\delta_a}$

4.2 Augmentation Stability by Propellers

When there exists a yaw rate, the velocities of propellers that are not in the symmetry plane are different, which will make a thrust increment relative to the produced benchmark. Furthermore, due to the large aspect-ratio, the additional directional damping derivative induced by propellers is large, thus the stability of spiral mode and the damping ratio of Dutch mode are also increased. [9]

The stability of the Dutch mode decreases with the increment of altitude and velocity, so the differential power of propellers must be adopted for the lateral augmentation stability. In order to improve propulsion efficiency, the wide-chord large diameter fixed pitch propeller, which has large inertia of moment, is usually applied in solar powered HALE UAVs, and the remaining power of the motor is small, thus the response of the differential power control is longer than conventional aerodynamic control surfaces, which will weaken the efficiency of differential power control augmentation stability system.

According to the mathematical model of motors and propellers, the dynamic system consisting of motors and propellers can be simplified into the 1st order inertia system. So the control law of the differential power stability augmentation system can be expressed as:

$$\delta_d = \frac{-a_1}{S - a_1}(K_\beta \beta + K_r r) \tag{17}$$

where δ_d is the differential power control command for the propeller; the first term of the right side of the equation is the dynamic model of the propulsion system; a_1 is the time constant of the system, and its specific expressions can be seen in Ref.[16]. Since the velocity of a solar powered UAV is not high and the feedback control gain of the propulsion inner controller is not large because of the power limitation, a_1 can be simplified as:

$$a_1 \approx -C_p \rho \frac{d^5}{4\pi^3} \omega / I_r \tag{18}$$

where C_p is the power coefficient of the propeller; d, ω, I_r is the diameter (m), rotation speed (rad/s) and the moment of inertia (kg.m^2)of the propeller respectively. From the above equation, a_1 is proportional to ρ, so the effect of differential power control at high altitude which is much more essential becomes inefficient. Substituting specific values into Eq. (18), a_1 = -0.33 (1/s) can be calculated for the UAV in the cruise phase. From the principles of automatic control, the settling time of the system is about 9 seconds, and the cutoff frequency is 0.33rad/s, which is even lower than the natural frequency of the Dutch mode of the UAV.

To quantify the impact of the dynamics of power system on the lateral-directional dynamics, the same parameters of K_r = 4 and K_β= -2.6 in feedback controller is adopted. The Lat-Dir root locus and Bode diagram are plotted with and without the consideration of the dynamics of power system that are formulated in Eq. (17)~(18), the results are shown as follows:

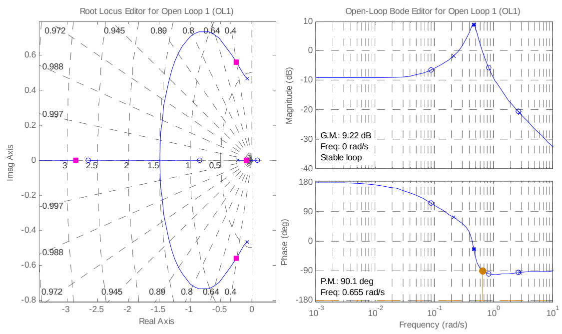

(a) Without considering the dynamic aspects of the power system

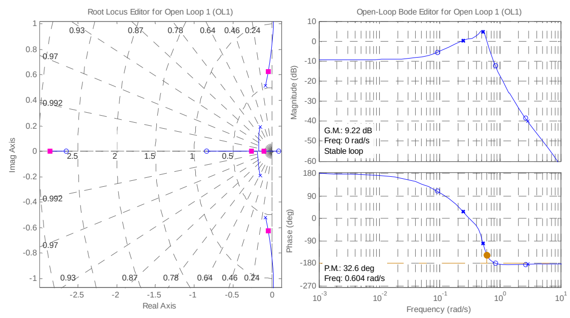

(b) Considering the dynamic aspects of the power system

Fig.13 Lat-Dir root locus and Bode diagram

Concluded from the above figures, the phase margin declines about 60 degrees and the damping ratio of the Dutch mode drops from 0.4 to 0.08 using the same control law after considering the dynamics of the power system. Thus, when applying differential power systems for lateral control augmentation, the efficiency of control may be seriously deteriorated because of the impact of the inertia of propulsion system.

5 Conclusion

The LQG/LTR control method with all wing span elevons is suitable for the pitch control of highly flexible solar-powered UAV, since it needs less measurable variables to provide a quick dynamic response with very small additional deformation of the wing.

Due to the large lateral static stability and poor directional static stability, the lateral control efficiency of elevons of high aspect-ratio straight flying wing solar powered UAV is very limited, and the roll control tends to reverse, no matter the wing is rigid or flexible.

When cruising at high altitude, the propulsion system's cut-off frequency is lower than the natural frequency of Dutch mode. As a result, when using the differential power for lateral-directional augmentation stability control, the inertia of propulsion will significantly reduce the phase margin and the damping ratio of Dutch mode.

References

[1] Mayuresh J. Patil. *Nonlinear aeroelastic analysis, flight dynamics, and control of a complete aircraft*. Ph.D. Dissertation, Georgia Institute of Technology, Atalnta, GA, May, 1999.

[2] Mayuresh J. Patil, Dewey H. Hodges. Flight dynamics of highly flexible flying wings. *Journal of Aircraft*, Vol. 43, No. 6, pp 1790-1798, 2006.

[3] Raghavan, B. and Patil, M. Flight dynamics of high aspect–ratio flying wings: effect of large trim deformation. *AIAA 2007–6386*.

[4] Brijesh Raghavan, Mayuresh J. Patil. Flight dynamics of high-aspect-ratio flying wings: effect of large trim deformation. *Journal of Aircraft*, Vol. 46, No. 5, pp 1808-1812, 2009.

[5] Su, W. and Cesnik, C. E. S. Dynamic response of highly flexible flying wings. *AIAA Journal*, Vol. 49, No. 2, pp 324-339, 2011.

[6] Christopher M. Shearer, Carlos E. S. Cesnik. Nonlinear flight dynamics of very flexible aircraft. *Journal of Aircraft*, Vol. 44, No. 5, pp 1528-1545, 2007.

[7] Henrik Hesse, Rafael Palacios, Joseba Murua. Consistent structural linearization in flexible aircraft dynamics with large rigid-body motion. *AIAA Journal*, Vol. 52, No. 3, pp 528-538, 2014.

[8] Wang Rui, Zhou Zhou, Zhu Xiaoping, Xu Xiaoping. Flight dynamics of highly flexible solar-powered UAV based on geometrically nonlinear intrinsic beam. *ICAS 2014*. St. Petersburg, Russia, Vol. 1, pp 1-11, 2014.

[9] Wang Rui, Zhu Xiaoping, Zhou Zhou. Research on lateral-directional flying quality of multi-propeller solar powered UAV. *Flight Dynamics*, Vol. 30, No. 1, pp 5-8, 2012. [Chinese]

[10] Rafael Palacios, Joseba Murua, Robert Cook. Structural aerodynamic models in nonlinear flight dynamics of very flexible aircraft. *AIAA Journal*, Vol. 48, No. 11, pp 2648-2659. 2010.

[11] David A. Peters, Swaminathan Karunamoorthy, Wen-Ming Cao. Finite state induced flow models; part i: two-dimensional thin airfoil. *Journal of Aircraft*, Vol. 32, No. 2, pp 313-322, 1995.

[12] Jan R. Wright, Jonathan E. Cooper. *Introduction to aircraft aeroelasticity and loads*. Second Edition, John Wiley & Sons, Ltd, 2015.

[13] Rui Wang, Zhou Zhou, Xiaoping Zhu, Xiaoping Xu. Distribution control of large scale highly flexible solar-powered UAV. *Mathematical Problems in Engineering*, Vol. 2015, No. 1, pp 1-13, 2015.

[14] Athans M. A tutorial on LQG/LTR method. *Proe. American Control Conference*, Seattle, 1986.

[15] Gao Hao, Zhu Peishen, Gao Zhenghong. *Advanced flight dynamics*. Beijing, China: National Defense Press, 2004. [Chinese]

[16] Xiao Wei. *Research of flight dynamics and control for high altitude solar-powered UAV*. Xi'an, China: PH.D Dissertation of Northwestern Polytechnical University, 2012. [Chinese].

6 Copyright Statement

7 Contact Author Email Address

Rui Wang: wangrui@nwpu.edu.cn
Xiaoping Zhu: zhouzhou@nwpu.edu.cn